# Dissecting Atomic Interweaving Friction Reveals the Orbital Overlap Repulsion and Its Role on the Integrity of Woven Nanofabrics in Composites

*Mohammad Zakertabrizi[1], Ehsan Hosseini[1], Hamed Fallahi[1], Terry Creasy[2], Ali Tabei[3], Amir Razmjou[4], Kenan Song[5], Kyungjun Lee[6], Dorrin Jarrahbashi[1], Amir Asadi*[2,7]*

[1] J. Mike Walker '66 Department of Mechanical Engineering, Texas A&M University, College Station, Texas 77843, USA
[2] Department of Materials Science and Engineering, Texas A&M University, College Station, Texas 77843-3367, USA
[3] School of Mechanical, Industrial and Manufacturing Engineering, Oregon State University, Corvallis, OR 97331, USA
[4] Centre for Technology in Water and Wastewater, University of Technology Sydney, New South Wales 2007, Australia
[5] The School of Manufacturing Systems and Networks (MSN), Ira A. Fulton Schools of Engineering, Arizona State University, Mesa, AZ, 85212 USA
[6]Department of Mechanical Engineering, Gachon University, Gyeonggi-do 13120, South Korea
[7] Department of Engineering Technology and Industrial Distribution, Texas A&M University, College Station, Texas 77843-3367, USA

Email address: amir.asadi@tamu.edu

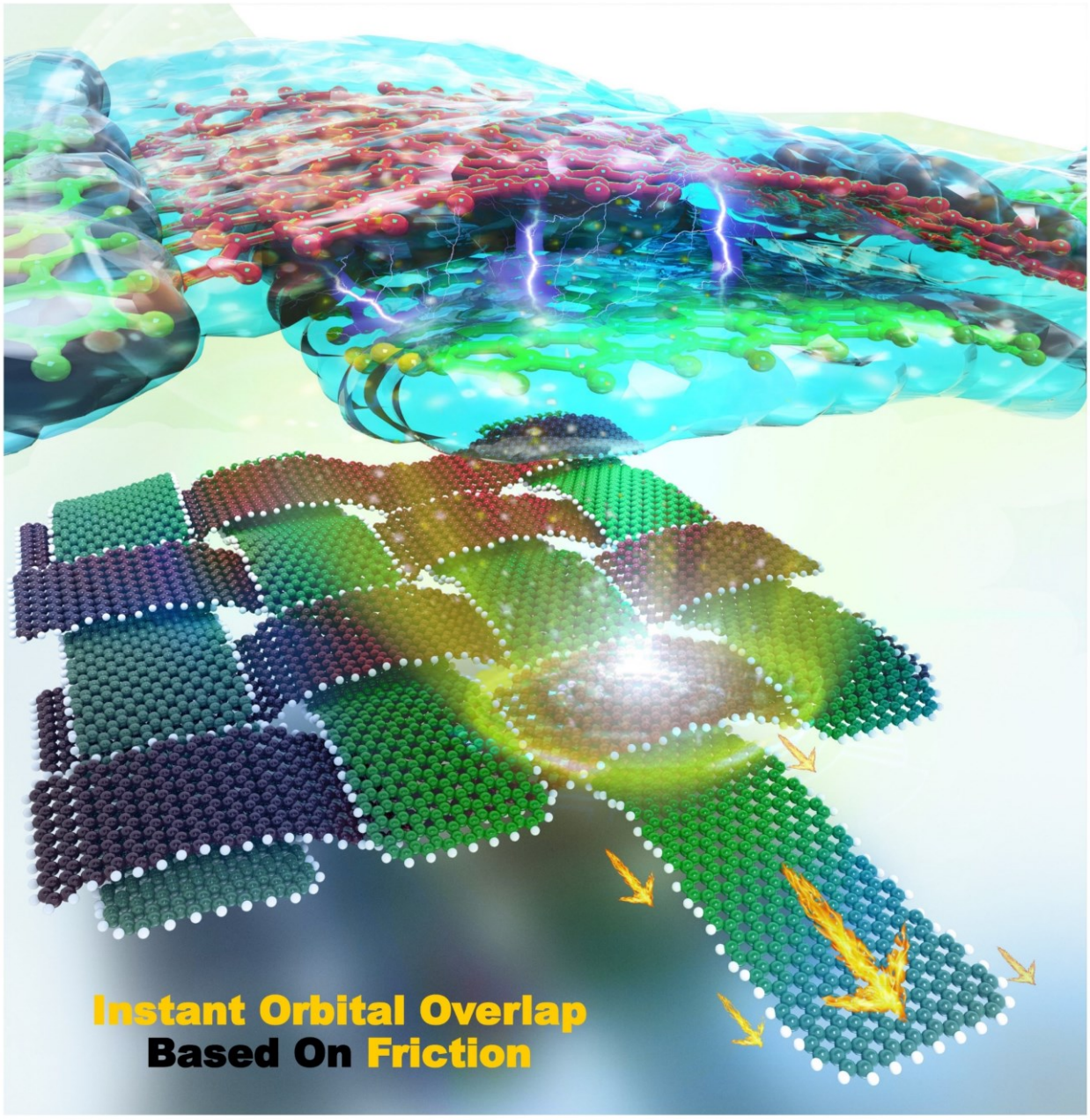


**Graphical insight**

## Abstract

Strong and stable woven formations are a type of promising structure for regulating external forces in hybrid materials system with desired electro/thermomechanical properties. The strength of the knitted composite structures relies on the distribution of stress over a cohesive network of nanoribbons/fabrics, whose integrity is dependent upon an underlying mechanism of stabilization through friction that keeps the nanoribbons/fabrics in their place. Herein, we uncover a new molecular-level friction mechanism in interwoven composite structures, where the extreme pulling speed causes instant orbital overlap, which creates additional resisting interfacial shear strength that delays the collapse of the woven structure. Our theoretical analysis of atomic woven two-dimensional materials (e.g., graphene, Mxene, black phosphorus, and Layered Double Hydroxide) conducted through Molecular Dynamics simulations and Density Functional Theory calculations help breakup this force between the atomic interactions and a repulsive force residing within the forced orbital overlap at the edges of the sliding and the confining nanosheets. Our results depict the robustness of the epoxy-weave interface considering the presence of imperfections within the woven formation. The detailed dissection of the friction within the woven formations provides new insight into its crucial role in preserving the post-failure integrity of woven composites. This knowledge will help understand the physical behavior of knots and weaves as reinforcements at the atomic scale and further in realizing the potential of nano fabrics for bottom-up ultimate design.



**Keywords:** Graphene woven nano-fabric; Graphene nanoribbons; Molecular dynamics simulation; Density Functional Theory; Pull-out strength; Interwoven friction.

## Introduction

Potentially essential to bio-imitating efforts, graphene is a formidable material with robust mechanical properties and substantial chemical and physical stability [1-7]. These qualities have quickly brought it into the spotlight after its initial introduction in 2004 [8]. Graphene, along with its 1D counterpart CNT has been one of the base materials for multiscale studies [9-13]. Other nanoparticles, such as boron nitride nanosheets (BNNS), are also appreciated due to their distinct electrical and thermalproperties and are used in composites [14-17]. Still, the size limitations of nanosheets and their production process-induced damages are major obstacles to their use in macroscale applications. One way to take advantage of the considerable properties of 2D nanomaterials in macroscale while avoiding their inevitable post-manufacturing defects, is to integrate them into weaves [18, 19], which has been made possible through recent advances such as stretching [20] or lifting [21] a single molecular wire. This way, the van see Waals (vdW) interactions and geometrical constraints create a large semi-isotropic sheet with strong cohesion and high toleration for tears from either direction [22-25]. The weave, in various forms of over-under crisscross patterns, is controlled by the same forces that control the nanolayer–nanolayer friction. Although generally viewed as a disadvantage, this friction forms the basis for woven nanostructures by limiting the movement of the ribbons in the weave and preventing warps and wefts from sliding and the weave from de-bundling.

Theoretical means in form of simulations have been an indispensable tool to probe physical and chemical mechanisms at microscale [26-33]. Most of the literature on the friction of nanosheets hovers around using nanosheets to create an ultra-low-friction state to benefit from their outstanding lubrication property [34-37]. For instance, Zheng et al. studied the proper alignment of graphene on a Ge(111) substrate to preserve the ultra-low level friction even after fluorination or oxidation [38]. In another study, Vazirisereshk et al. characterized friction over graphene and $MoS_2$ at the nanoscale using atomic force microscopy (AFM) and further examined in molecular dynamics (MD) and density functional theory (DFT) calculations [39, 40]. Other studies explored the nature of the friction and its relationship with the normal force, displacement and the morphological features of the sliding surfaces [41-44]. The theoretical approach to the friction force

have contributed its production to the Coulomb forces offset by vdW gravitation [43]. The sparse studies on this subject have observed the woven graphene sheet to be mechanically as robust as singular graphene nanosheet and reliable, as it removes the concept of critical bonds in the face of tearing stress [18, 19]. Still, post-failure stability in the weave, when after a possible ribbon rupture the friction becomes the dominant stabilizing factor, remains unexplored.

Herein, we address the friction effect in two-dimensional nanomaterials when a nanoribbon/fabric is pulled-out of the weave due to tensile forces. Applying this kinetic energy causes a surge in the resisting forces, which we observe through MD simulations, that prevents the formation from instantly falling apart. We use quantum mechanics/molecular mechanics (QM/MM) calculations to explore the attractive/repulsive nature of the interactions that form the basis of the resisting forces during forced movements from multiple directions. However, limited computational capacity has restrained the scope of simulations to extreme loading conditions, with several orders of magnitude higher sliding velocity than observable experimental setup [45]. Still, the higher sliding speeds can be perceived as the initial phase of failure, where a ribbon is suddenly ruptured and starts sliding within the weave. The data from simulations can be used to observe the behavior of complex woven formations under extreme loading conditions, where friction elemental to the continued cohesion of the formation. These data shed light on the effect of atomic scale friction within woven nano fabric reinforcements and their effect on the integrity of the entire composite structure at higher length scales.

## Method

A quantitative analysis of friction and pull-out interactions in woven shapes of two-dimensional nanomaterials was conducted using MD, QM/MM and DFT simulations.

### Molecular Dynamics

In MD simulation, three patterns of woven, plain, twill, and satin are designed for Graphene, Mxene, Black phosphorus, and Layered Double Hydroxide as two-dimensional nanomaterials. The COMPASS forcefield

[46-50] modeled the atomic interaction for each graphene and black phosphorus structure. Also, for using a reliable forcefield for Mxene and Layered Double Hydroxide, we used the Universal forcefield [51-54] and the INTERFACE forcefield [55-57], respectively. The forcefields considered in this study have all been demonstrated to be applicable when describing mechanical properties. Furthermore, forcefields have been employed to investigate interfacial properties and interactions with different materials.

The woven shape was created by overlaying ribbons for each woven pattern. For the plain pattern, four ribbons are woven in the X and Y directions, and for the twill and satin patterns, because a larger weave is required to fully consider the skips, we applied six ribbons in the X and Y directions. The size of ribbons for all two-dimensional material follows two coordinates; the size of small models is 120 Å and 20 Å in the length and width of each ribbon (figure 1a-d and figure 2). For the large model examined in Figure 5, we used ribbons with sizes 170 Å and 25 Å in the length and width, respectively[58, 59].

In the first stage, models are subjected to geometry optimization, and then under NVT ensemble (a constant number of particles, constant volume, and temperature dynamics simulation) is employed to optimize the woven shape and relax the system for 400 ps (The sides of the ribbons are fixed in the X and Y directions). Then the ribbons are assigned a speed *Vx* and a NVE ensemble (a constant number of particles, constant volume, and energy dynamics simulation) is conducted. The speed *Vx* of ribbons is extracted under different sliding distances δ. Based on *Vx*, the loss of global kinetic energy ($\Delta E_{kinetic}$) of the ribbons during sliding is computed as in equation (1) [50, 60]:

$$\Delta E_{kinetic} = \frac{1}{2} m\left(v_x^2(\delta) - v_x^2(\delta_0)\right) \qquad (1)$$

Where *Vx (δ0)* is the average speed of all the atoms of the ribbons after being assigned an initial speed, is the average speed of all the atoms of the ribbons after sliding, and m is the mass of the ribbons.

The friction force is then calculated as in equation (2):

$$F = \frac{\Delta E_{kinetic}}{\delta} \qquad (2)$$

117 The interfacial shear strength τ can be given by the equation (3):

118 $$\tau = \frac{F}{A} \qquad (3)$$

119 Where *A* is the area of the ribbon. (more information is available in supplementary)

120 **Mechanics/Molecular Mechanics (QM/MM)**

121 To explore the impact of electron effects on friction, we conducted a series of simulations using the
122 Quantum Mechanics/Molecular Mechanics (QM/MM) approach through the QMERA method,
123 implemented in Materials Studio. Our investigation involved two-layer QMERA models, where the total
124 enthalpy of the system is defined in equation (4) as follows:

125 $$\mathrm{H(QMERA)} = \mathrm{H(H,SL)} + \mathrm{H(M,IL)} - \mathrm{H(M,SL)} - \mathrm{H(L,IL)} \qquad (4)$$

126 Here, H, M, and L denote high, medium, and low levels of theory, while SL, IL, and RL represent small,
127 intermediate, and real layers of the system. In our study, the small and intermediate QMERA layers were
128 scrutinized using quantum mechanical methods, whereas the Universal force field was employed for the
129 real layer. The nature of stationary points was confirmed through vibrational frequency analysis.

130 The small layer and medium layer consisted of 498 atoms in the QM region, while the real layer in MM
131 contained 2310 atoms, forming stacked ribbons. In the three-layer model, the QM region was analyzed
132 using PBE-D3, demonstrating its capability to model dispersion interactions. The basis set employed was
133 DNP (Double Numerical plus polarization) with the addition of diffuse functions, ensuring good accuracy
134 for cases requiring such functions and orbital cutoff set at 4.6 Å [61-66] (Figure 4 and Figure 7).

135 **Density Functional Theory**

136 The spin-unrestricted density functional theory (DFT) calculations were performed using the DMol3 code.
137 This method is based on using charge density ρ to calculate all ground-state properties, among them the
138 total energy $E_t$, as shown in equation (5) [67]:

139 $$E_t[\rho] = T[\rho] + U[\rho] + E_{xc}[\rho] \qquad (5)$$

Where T[ρ], U [ρ] and $E_{xc}$[ρ] are the kinetic energy of non-interacting particles, the electrostatic energy due to Coulombic interactions and the exchange-correlation functional (remaining electronic energy not included in the other two terms), respectively. The first two energy components can be written as (6) and (7) [68]:

$$T = \langle \sum_{i}^{n} \phi_i \left| -\frac{\nabla^2}{2} \right| \phi_i \rangle \qquad (6)$$

$$U = \int V_N(r)\, \rho(r) dr + \frac{1}{2} \int \frac{\rho(r_1)\rho(r_2)}{|r_1 - r_2|} dr_1 dr_2 + V_{NN} \qquad (7)$$

For (7), separate terms describe electron-nucleus attraction, electron-electron repulsion and nucleus-nucleus repulsion. In an orbital basis set, the charge density over all occupied molecular orbitals at position r can be obtained from equation (8) [69]:

$$\rho(r) = \sum_{i} |\phi_i(r)|^2 \qquad (8)$$

Where $\phi_i$ are the charge densities of a set of fictitious, orthonormal orbitals at position r. Exchange-correlation functions were determined employing a uniform generalized gradient approximation (GGA) and the revised Perdew−Burke−Ernzerhof (PBE-D3) method.[70] Core treatments utilized the all-electron relativistic (AER) procedure, explicitly taking into account all core electrons and introducing specific relativistic effects into the core. The selected basis set was double numerical plus polarization (DNP), with an orbital cutoff set at 4.6 Å.[13, 71]

The primary ribbon was crafted with a length of 112 angstroms and a width of 7 angstroms, featuring four smaller ribbons with dimensions of 21.3 angstroms in length and 17.5 angstroms in width, each. The atoms within the side region (highlighted in red) of the smaller ribbons were immobilized to prevent the displacement of ribbons resembling a bulk model.

The system was optimized to achieve lower energy and relaxation. To simulate pullout, we employed a dynamic simulation lasting 5 picoseconds, during which the larger ribbon (highlighted in yellow in Figure 6f) pulled out from the smaller ribbons at varying speeds (0.1, 1, 5, 10 km/s).

## Results and discussion

### Initial Friction analysis in woven fabrics

Weaving forms a near homogenous network of nanosheets, which covers the sheets' defects and unifies them into a larger singular sheet capable of distributing stress more uniformly along its surface. To track the effect of woven form, we used four different nanosheets with different properties as nanoribbons. In this study, we describe ribbons as long 2D nanosheets. These nanosheets are graphene, Mxene, black phosphorous, and Layered Double Hydroxide (LDH), shown in plain woven formation in Figures 1a-1d, respectively. We chose these materials because of their popularity in nano constructs beholden to their electrical, mechanical and chemical prowess. The outstanding properties of the nanosheets in this scale can be extracted in a homogenous structure if their movement is restricted inside the weave. In their usual formation, exfoliation is possible due to the weak vdW forces in the interlayer region, as shown in Figures 1e-1h. Herein, the axial distance and the interlayer distance, i.e., the distance between the axis of two consecutive layers and the smallest distance between neighboring nanoribbons, are marked. These values correspond with the values in the literature for graphene [72], Mxene [73, 74], black phosphorous [75, 76] and LDH [77]. It can be seen that the interlayer distance corresponds with the strength of interlayer interactions that resist sliding. Typically, the interactions remain non-bonding with no orbital overlap (Figures 1ei-1hi). The layered formation with constant interlayer distancing means minimum resistance against sliding. The restrictions on the movement in the woven form are represented by the effort required to pull out the nanoribbons from within the weave. This is parametrized in changes in the sliding speed, or the rate by which the pulled nanoribbons is displaced within the weave (i.e., displacement rate). For instance, Figures 1i-1l depict the relationship between the initial sliding speed and the resisting force per contact surface area, i.e., friction per contact area. With the initial sliding speed (i.e., displacement rate),

increasing from 0.1 to 10 km/s, the resisting force per contact area soars from ~10 to ~1000 MPa. Sliding happening at significant speed demonstrate the possible state of failure in exceptional situations where one (or more) nanoribbons subjected to extreme loading fails and leaves the preservation of the stability of the weave to the friction between the failed ribbon and its confining counterparts. This is shown in Figures 1i-1l. The high shear strength (friction force per contact area) in the plain pattern indicates that the friction is directly related to the number of edges involved "over-under" in a specific weaving pattern, which does not exist in the stacked formation. That is, the resisting force in the interacting edges, called the interweaving, exists irrespective of the base material, which determines its magnitude. Increasing the initial sliding speed greatly intensifies the interactions at the edges, where the movement path for the moving nanosheet creates an angle with the pull out direction. The interfacial shear strength grows as a direct result of the upsurge in the engagement at the edges. Therefore, it can be hypothesized that involving more interacting edges in the woven structure can further solidify the nanosheets in a woven form compared to a stacked form. This is especially important, since high initial speed in the formation that happens in the event of a major failure scenario can come with significant ruptures in the nanosheets, creating more interaction edges, thus resulting in higher sliding shear strength and delayed failure.

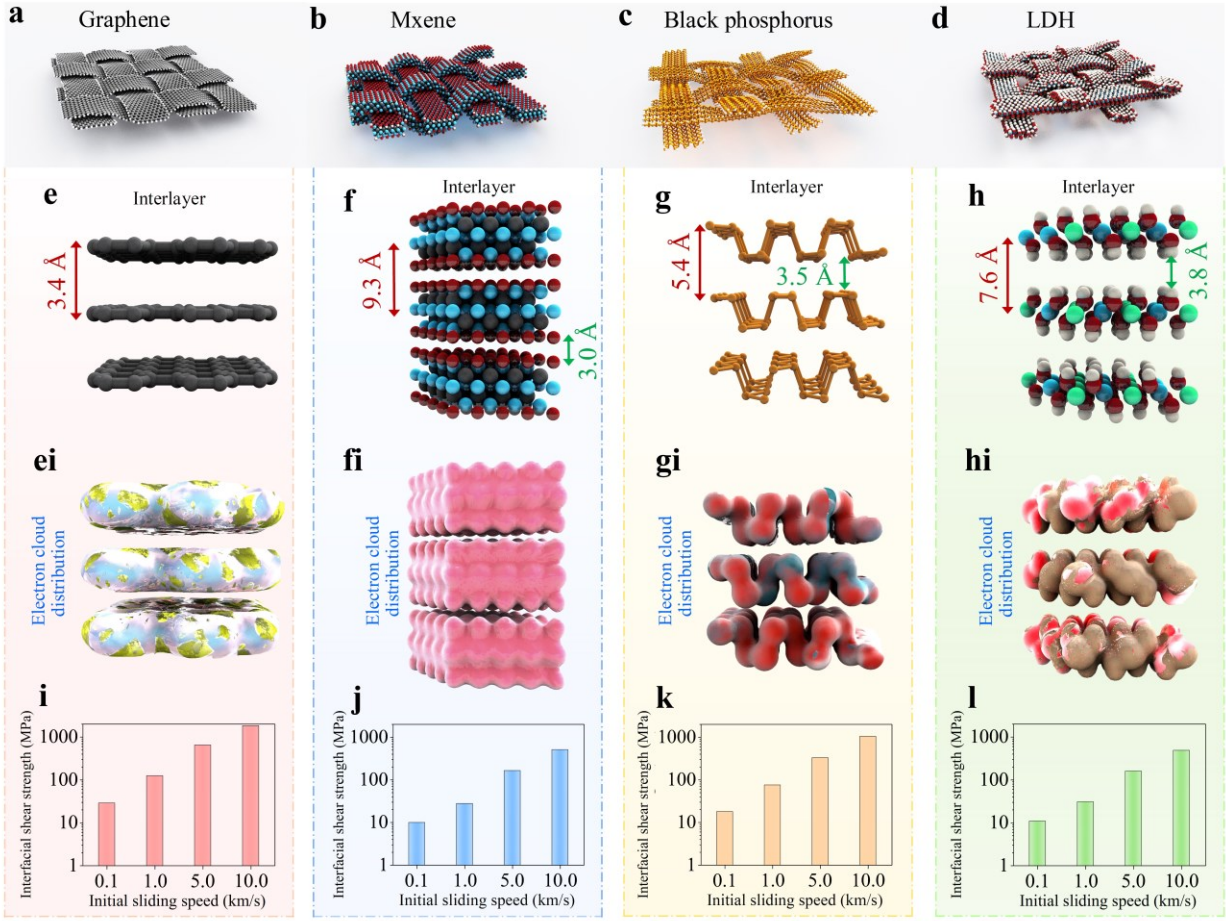


*Figure 1. The molecular woven plain pattern of (a) graphene, (b) Mxene, (c) black phosphorus, and (d) Layered Double Hydroxide. Layered structure of (e) graphene, (f) Mxene, (g) black phosphorus, and (h) LD with their electron distribution in (ei) graphene, (fi) Mxene, (gi) black phosphorus, and (hi) LDH. The interactions between neighboring layers remain non-bonding, and their electron clouds are separate. Interfacial shear strength, i.e. friction per contact area, for (i) graphene, (j) Mxene, (k) black phosphorus, and (l) LDH show that as the initial sliding speed increases, the pulled-out nanosheet's resistance grows stronger.*

Graphene was chosen to represent all other nanosheets to address the multivariate question of the woven formation of 2D nanoribbons. The woven patterns include several forms, the most prominent forms of which are brought in Figure 2. These are the plain form (Figure 2a), twill form (Figure 2b) and the satin

form (Figure 2c) also shown in Figure S1 in the supplementary file. The plain form follows a basic crisscross pattern, forming a checkerboard style with weft nanoribbons going over and under warp nanoribbons. In the twill form, the weft thread goes over and under multiple, here two, warp nanoribbons in an alternating sequence. In the satin form, the weft goes over three warp nanoribbons, then passes under one weft thread before repeating the process again. The relative positioning of the ribbons is especially important for the determination of the final cohesion between the ribbons, which prevents failure both from external forces or the independent movement of ribbons that disassembles the weave. Herein, the movement paths are marked to show the possible routes for the ribbons that can lead to the weave being disassembled. Due to the substantial mechanical properties of graphene, these movements can be considered the critical mode of failure for the weave. Therefore, exploring the possibility of sliding and the preventive mechanisms are the key to the strength and stability of the nanoscale weaves.

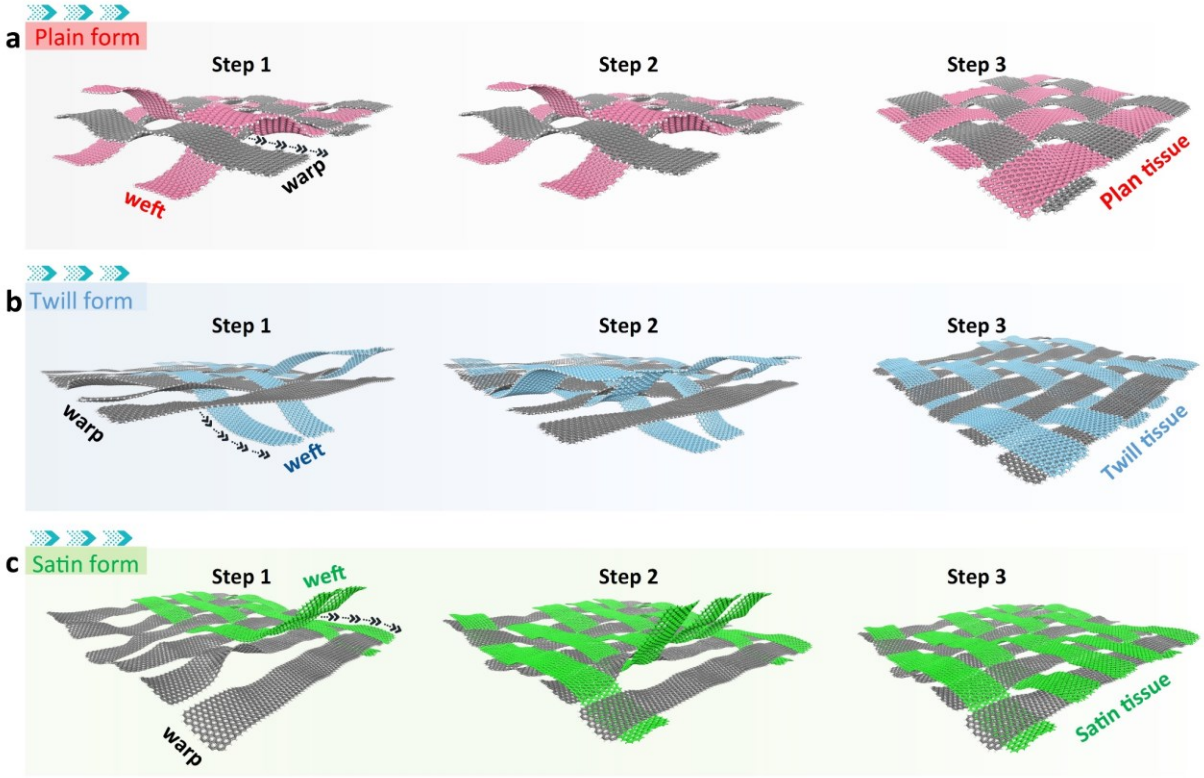


*Figure 2. Woven patterns are (a) plain, (b) twill, and (c) satin forms. The plain form follows an over-under pattern without skips. The twill and satin forms follow a similar pattern but with one and two skips,*

*respectively. While the interacting area is similar, the interacting edges decrease with the skips. These steps show the collapsing woven form as the nanoribbons are pulled out.*

**Effect of weaving patterns on sliding speed-sliding distance relationship**

Although the stress distribution over the entire network is the main mechanism for bearing loads in woven structures, it is the mechanical grip/interlocking that keeps the woven network together. Therefore, the main failure for the woven structure is not through direct mechanical stress but a pull-out motion applied on one or more of the nanoribbons. An unhindered pull-out motion means losing a support for an array of parallel nanoribbons, which negatively impacts the cohesion of the weave. Therefore, the effectiveness of woven patterns in preserving the weave can be compared through their respective success in obstructing or slowing down the pull-out process. The resistant interfacial shear strength, which is the principal parameter for evaluating the cohesion of the weave, is characterized by the changes in the initial pull-out speed and the strain rate, i.e. change in the directional strain of the nanoribbon during pull-out, as the nanoribbon is displaced within the weave (Figure 3a). The results are shown in Figures 3b-3d, where the difference in the pull-out speed and the corresponding strain rate for three different woven forms of graphene are depicted against the corresponding displacement. The drop in the initial sliding speed can represent the gradual activation of the intertwinement mechanism that keeps the ribbons in their place.

As a result of activating this friction, which is absent from the simply stacked nanosheets that show nearly constant sliding speed, the initial sliding speed drops significantly with increasing displacement. This translates into a significant stabilizing potential in face of failure, particularly in extreme loading conditions. For the woven ribbons, further movement of nanoribbons hinders the sliding speed (Figure 3b-d). With the 1 Å/s initial speed, the drop is 0.075 Å/s (7.5%) as the displacement grows to 20 Å; whereas in the 10 Å/s and 100 Å/s, the drop is 1.5 Å/s (15%) and 15 Å/s (15%), in the similar displacement respectively. Evidently, higher initial sliding speeds are faced with higher speed drops, meaning larger opposing forces. However, the share of the drop in the model with the lowest initial speed (1 Å/s) is nearly half that of the models with the initial speeds of 10 and 100 Å/s. This means that the form of the applied friction changes

at higher speeds. The responsible phenomenon here, called the interweaving friction, or the overlapping grip, forms at the edges where the moving nanoribbon slides between the two confining nanoribbons. This mechanism is further examined through the QM/MM method.

In short, a close look at the sliding resistance force/interfacial shear strength of different weaves in Figures 3b-3d shows that while satin and twill forms follow the same semi-linear pattern, the pull-out resistance in the plain form depicts a lower sliding speed. This can be translated to higher pull-out resistance and interweaving friction, resulting from higher confinement in the plain form. In other words, the greater number of over-under patterns in the plain form can be a contributing factor to its higher pull-out resistance.

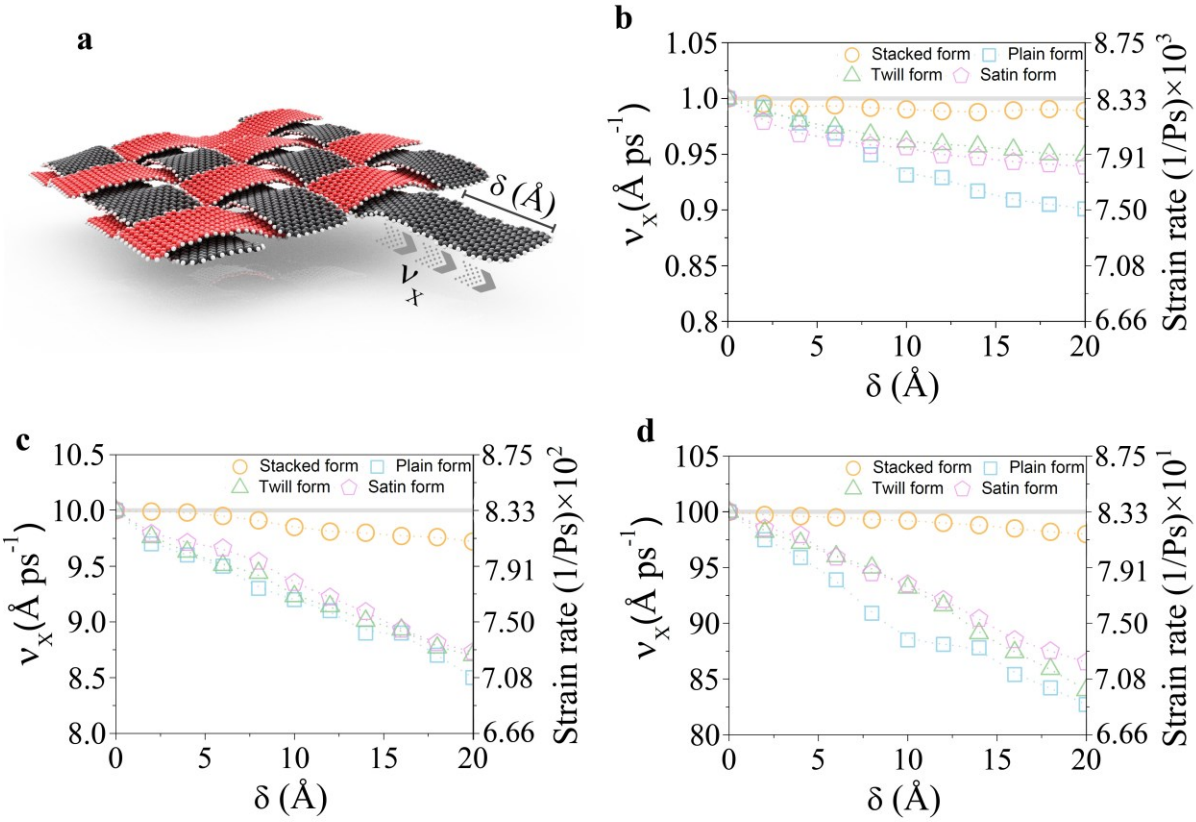


*Figure 3. (a) pull-out/sliding process. Pull-out speed is depicted against pull-out distance for initial speeds of (b) 1 Å/ps, (c) 10 Å/ps, and (d) 100 Å/ps. δ is sliding distances; it shows the measured distance of the*

*nanoribbon that has been pulled out of the weave. The corresponding speed of the ribbon is depicted as v, which tracks a declining path as the resistance forces cause decelerate the movement of the ribbon.*

**Friction and the role of forced orbital overlap**

The sliding resistance patterns show that the plain pattern provides the highest interweaving friction necessary for preserving the weave structure. Tracking the stress throughout the length of the sliding nanoribbon marks the sections with the highest resistance caused by interweaving friction and provides grip. The stress path along the sliding nanoribbon, shown in Figure 4a, was analyzed with the results planned on each atom in Figure 4b, where the stress is depicted in a spectrum from white, no resisting force, to full red, $5.0\times10^{-2}$ nN, the highest resisting force. The resistance force values show the points of concentration to be the edges, where the sliding graphene is closely interacting with the other nanoribbons in the woven network. Three critical sections of the pulled graphene are separately depicted with respect to the stress levels. Figure 4b shows these areas, i.e., top (the first area), first grip (the second area), and second grip (the third area). Figures 4c-4e demonstrate the aforementioned areas regarding the stress level applied to the sliding nanoribbon's atomic structure. Exploring the highly stressed areas of the depicted sections, represented by green, reveals that the resistance stress in all three regions is concentrated in certain sections. Figures 4c-4e show that the resistance is mainly concentrated on the edges where the moving sheet is closely pressed towards the neighboring sheets. Here, the main lines of interaction, or grips, are clearly visible. From Figures 3b-3d, displacing of the pulled-out nanoribbon causes a drop in the sliding speed; this is a result of the forced spatial confinement in the interacting sections that cause interweaving friction.

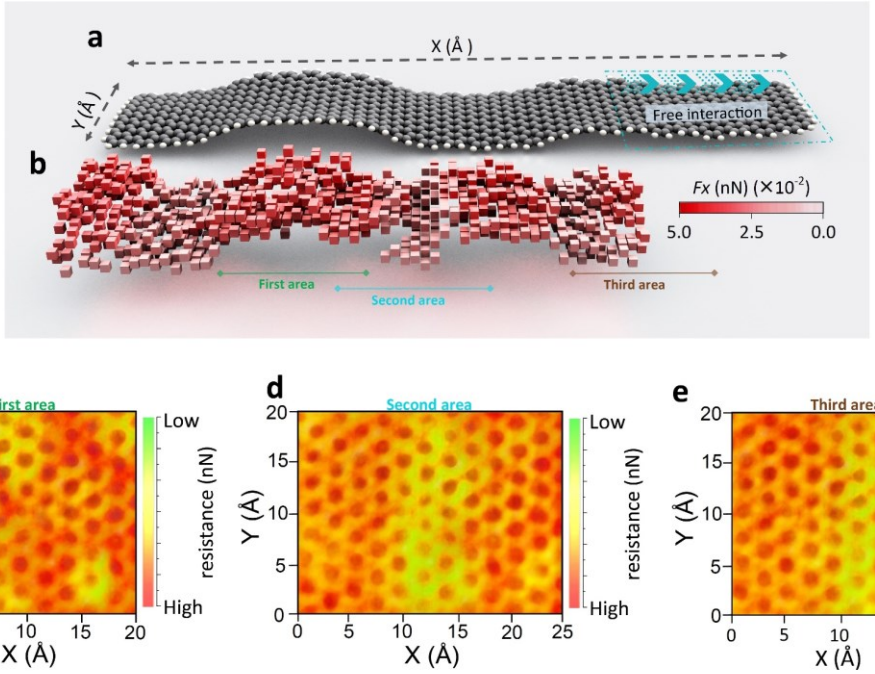


Figure 4. A scheme of the resisting forces mapped (QM/MM calculation) on the pulled graphene ribbon. (a) pulled graphene nanoribbon and (b) marked resisting forces marked for each atom. The main resisting sections are shown as (c) top, (d) first grip, and (e) second grip. The top section is where the nanoribbon goes over the bottom nanoribbon. The first and the second grip contain the edges, where the close interaction with the crossing nanoribbon creates a strong resisting force.

Considering the distribution of resisting forces over the length of the ribbon, Figure 4 depicts only a small section of the woven formation. More in-depth analysis is possible with the interweaving friction described over the sliding distance of the pulled-out nanoribbon. Figure 5 depicts the proposed interweaving friction on the sliding length of the graphene for different patterns and sliding speeds.

Figures 5a-5c show the friction forces for the three plain, twill, and satin patterns, respectively, with the sliding graphene ribbon pulled out at 1 km/s. The results show negligible friction force for all patterns. Still, the friction in the plain pattern is more distinctive than the others. Increasing the sliding speed to 10 km/s significantly highlights the stress patterns barely visible in Figure 5a-c. Here, a nanoribbon with a length of 170 Å is displaced by pulling out for a distance of 40 Å. While the differences in friction forces are not

visible in the lower sliding speed (1 km/s), multiplying the sliding speed by 10 km/s reveals concentrated friction forces at specific sections along the pulled nanoribbon (Figure 5d-f). Although the stressed spots closely resemble each other, the magnitude of the applied forces differs for each pattern. In general, friction forces are concentrated on the surfaces where the moving nanoribbon closely interacts with the other nanoribbons, which is in line with the observations from Figure 4. Now, the differences in the stress distribution can be clearly attributed to the physical surface contact between nanoribbons in different patterns. For instance, the plain pattern (Figure 2a) distributes the friction evenly between the interacting surfaces, adhering to the simple over-under pattern of woven nanoribbons. The interweaving friction is highest due to the maximization of the nanoribbon – nanoribbon interaction, whereby the edges are especially pressed against each other. In contrast, the twill and satin patterns show a more complex stress distribution. This is caused by the skipped steps of a simple repetitive over-under pattern. Smaller nanoribbon – nanoribbon interacting area and interacting edges result in lower interaction and the subsequent drop in the interweaving friction. Alteration in the stress distribution over the length of the sliding graphene is better depicted in Figure 5g-i, where the portrayed stress is extended over a larger scale in contrast to the smaller scale in the Figure 5d-f. The repetitive pattern of the interweaving friction is clearly visible in Figure 5g.

In contrast, the complex patterns of interweaving friction for the twill and satin forms show the importance of skipping over – under patterns in the weave. In the case of twill form, the graphene ribbon skips one ribbon before going under; this is evident in lower interweaving friction on the first ribbon, followed by a higher friction force on the second ribbon (Figure 5h). In satin form, sliding graphene skips over two ribbons (Figure 5i). Predictably, for each iteration of the weave, the first two experience lower stress than the third, which bears higher interweaving friction. As a result, the twill and satin forms are expected to provide lower collective interweaving friction and overall cohesion. Still, their woven pattern is more than enough to outperform stacked formations. Finally, these patterns resemble ordered friction pulses, demonstrating the areas where more friction is generated.

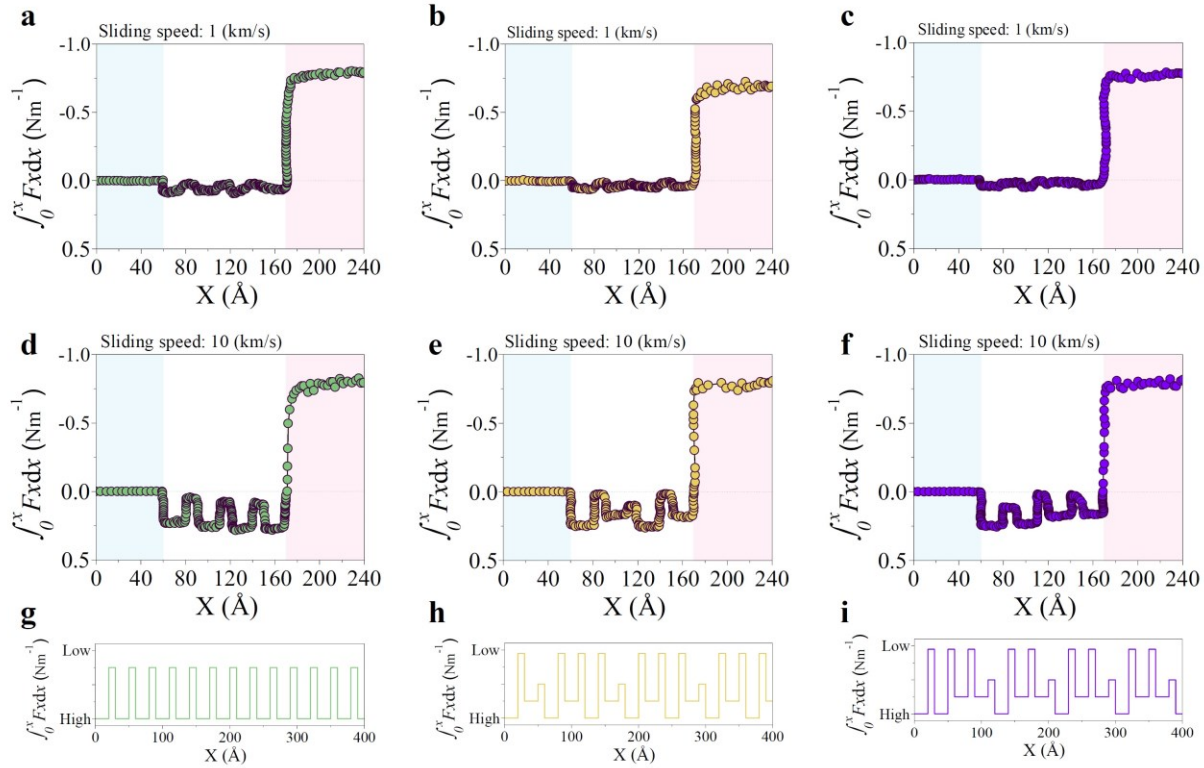


*Figure 5. Collective distribution of friction forces along the length of a graphene nanoribbon ($F_x$) in (a) plain, (b) twill and (c) satin weaves in unit width of the pulled nanoribbon, with the nanoribbon pulled at 1 km/s. Distribution of friction forces along the length of a graphene nanoribbon in (c) plain, (d) twill and (e) satin weaving, with the nanoribbon pulled at 10 km/s. Overall pattern of distributed friction force over the length of the pulled nanoribbon for (a) plain, (b) twill and (c) satin weave patterns.*

The collection of friction forces previously described in Figure 5 form the overall resistant force that prevents the pulled graphene ribbon from sliding. This resistance force, namely interfacial shear strength, increases with the sliding speed (and strain rates) for all models, including the stacked form (Figure 6a). That is, the vdW interactions in the stack form are able to resist the sliding to a certain degree. However, the resistance provided by the vdW forces is quite smaller than the interweaving friction, especially in the lower sliding speeds. As the applied force grows, and the initial sliding speed increases accordingly, the gap between the vdW friction and the interweaving friction grows smaller. This is better depicted in Figure

6b, where the relative magnitude of sliding resistance (shear strength) for the woven formations relative to the sliding resistance (shear strength) for the stacked formation drops from 8 to 2 as the sliding speed increases from 0.1 to 1.0 km/s. The higher shear strength remains nearly constant for 5.0 and 10.0 km/s pulling speeds; therefore, it can be hypothesized that the interweaving friction is more than three times the vdW stacked friction. This general advantage in pull-out resistance is well reflected in the total tolerated stress for the 10 and 100 Å/s sliding speeds shown in Figures 6c-6d.

Taking a closer look at Figures 6a-6b, the plain pattern consistently outperforms the twill and satin patterns of the woven form. The twill pattern also shows higher shear strength compared to the satin pattern. The higher shear strength is also visible in Figures 6c-6d, where the nanoribbon with plain pattern bears higher directional internal stress than the other two woven models. This gap grows wider from ~20 MPa or 25% to ~400 MPa or 28.5% of the stress in the satin pattern as the sliding speed increases from 10 Å/s to 100 Å/s. The superiority of the plain pattern lies within the interacting surfaces and edges. Complete over-under form, which is the case for the plain pattern, provides more edge – nanoribbon interaction spots. This interaction is especially important for interweaving friction as it applies a more effective grip than surface–surface vdW interactions. The nature of both interactions is further explored in Figure 7.

The resistive force responsible for the superiority of the woven formation over the stacked nanoribbons, as demonstrated by hybrid QM/MM approach, consists of attractive vdW forces and the proposed forced orbital overlap repulsive forces. Due to the nature of the orbital overlap repulsive forces, they are most accurately calculated from the comprehensive density functional theory calculations (DFT) as opposed to the atomic forces prioritized in molecular dynamics (MD). Given the hybrid nature of the QM/MM method used in this study, two sets of simulations in the DFT and MD setup were performed to isolate the effects of orbital overlap repulsion on the interfacial shear strength (Figure 6e). Due to the high computational cost of DFT calculations, this comparative analysis was performed on a simplified model of plain weave, as shown in Figure 6f. Since the resisting force (mapped in Figure 4) resides within the interacting edges and

surfaces, the relationship between DFT and MD results retains its significance regardless of the weave type or the ribbon size.

Figure 6e demonstrates the overwhelming presence of molecular interactions (isolated in the MD results) within the interfacial shear strength calculated in the DFT. The share of orbital overlap repulsion forces can be calculated as the difference between the results of MD from DFT calculations. While this difference as a share of the overall interfacial shear strength depreciates with increasing the sliding speed, it remains a significant portion of no less than 10% of the resisting force against sliding. The results from the QM/MM method retain a middle figure between MD and DFT, which attest to its accuracy considering the approximations used to accelerate the computation process.

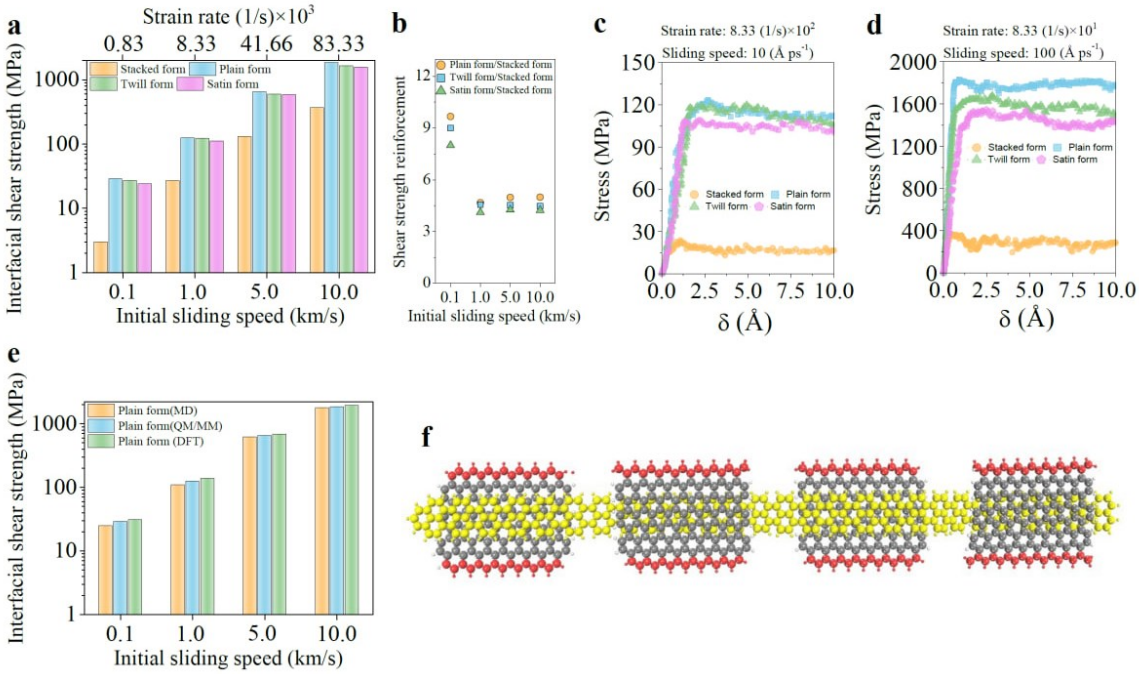


*Figure 6. Pull-out results depicting interfacial shear strength against the corresponding sliding speed for stacked, plain, satin and twill forms. (a) The interfacial shear strength and (b) shear strength reinforcement. Total internal stress tolerated by the pulled-out nanoribbon for (c) 10 and (d) 100 Å/s pulling out speed.*

*While the plain form outperforms the other patterns in interfacial shear strength at the initial phase and during the pull-out process, all woven patterns provide significantly higher friction stress. (e) Interfacial shear strength in different sliding speeds compared between MD, QM/MM and DFT analyses. (f) The isolated model analyzed in MD, QM/MM and DFT environments.*

Interactions in the woven formation strictly depend on the interaction surface and edges between the ribbons. These interactions keep the woven structure together by restricting sliding, as a deteriorating factor for the woven pattern. QM/MM calculation of the plain pattern shows the over-under form of the ribbons with their electron density cloud outlined (Figure 7a). In the stationary state, vdW interactions govern the intermolecular space (Figures 7a-7i), with little to no charge transfer taking place (Figures 7c-7e). Therefore, there is little to no difference between the stacked form and the weaves in terms of interactions.

Pulling a nanoribbon is met by the nanoribbon - nanoribbon vdW interactions shown in Figures 7a-7i, as well as a strong resistance caused by the forced overlap at the edges, where the moving nanoribbon is held in place by a shear force between two opposing nanoribbons from the top and the bottom (Figure 7b). QM/MM calculation shows that quick sliding caused by a robust pull-out force causes significant instantaneous electron sharing and the forced orbital overlap that significantly limits the nanoribbon's displacement (Figures 7b-7i). These repulsive interactions are the basis for interweaving friction.

The instantaneous sharing of the electrons due to the forced orbital overlap is accompanied by the transfer of charge between the nanoribbons as the sliding takes place. Tracking the transferred charges in each pattern can show the intensity of the forced interaction between the nanoribbons (Figures 7c-7e). The overall trend shows transferred charge growing with pulled distance for all weaving patterns. At the lowest sliding speed, 1 Å/s, the transferred charge remains near zero, which means the nanoribbon – nanoribbon interactions are in the form of vdW. As the pulling speed increases, the transferred charge grows and the interweaving friction appears in the form of forced orbital overlap. The friction peaks at 0.06 – 0.08 e at 100 Å/s in the plain pattern. The interweaving friction in the plain pattern demonstrates more than 33% higher transferred charge compared to the other patterns. This is a result of the additional interacting edges

in the plain pattern, as depicted in Figure 2, where the weft ribbon follows the over-under pattern without skipping over the warp ribbons.

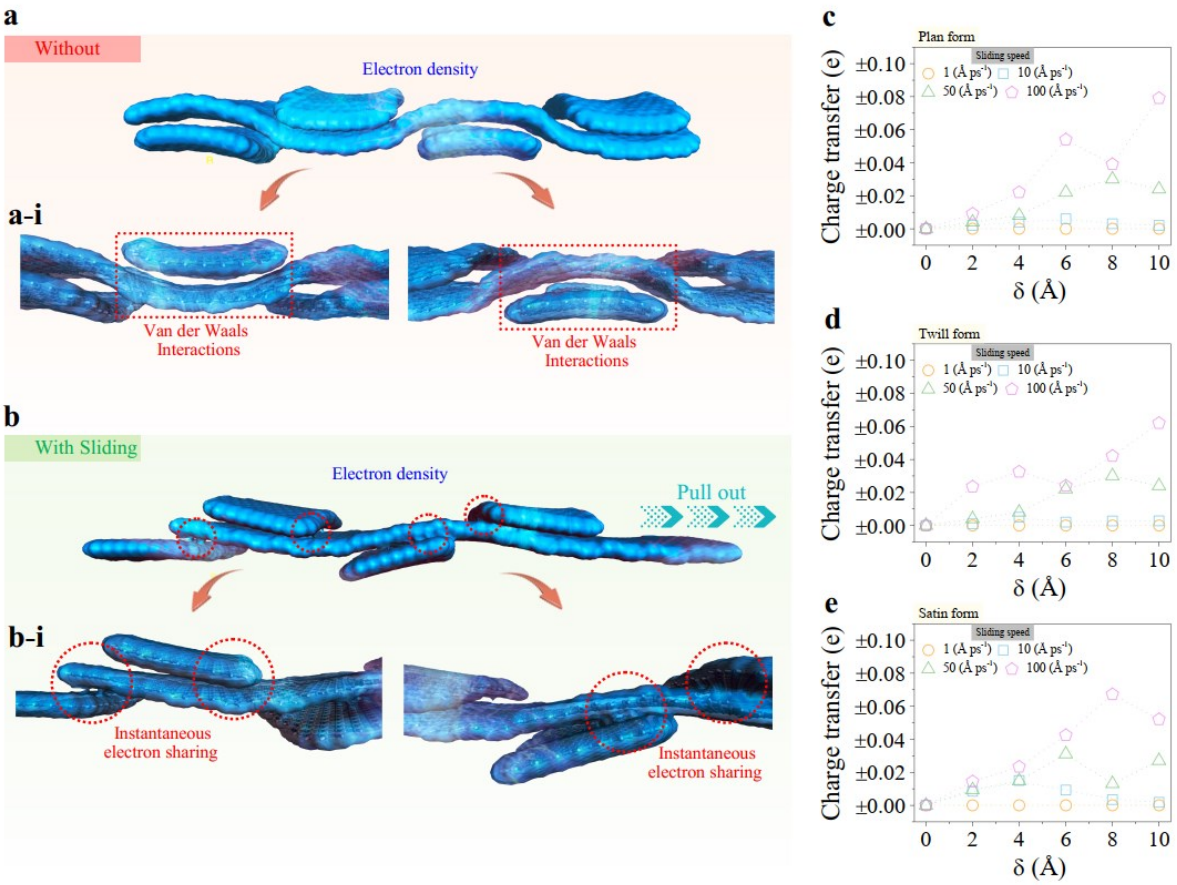


*Figure 7. Electron density at the (a) still and (b) sliding state. The interacting surfaces and edges are marked: when still, the main interactive sites between the ribbons are the covering surface area. After being pulled out, the repulsion from forced overlap in the interacting edges dominates the resisting forces. Charge transfer between molecules in (c) plan (d) twill (e) satin forms. As the graphene nanoribbon is pulled out through the woven formation, the transferred charge between the ribbons grows.*

**Reinforcing interactions**

The woven structure, especially on the macroscale, is accompanied by polymer materials to stabilize and improve the overall cohesion of the weave, forming a composite material. Still, the potential role of the

408 essential elements in the woven structure and the polymer–ribbon interactions and their contribution to final
409 mechanical properties remains elusive. The epoxy nanocomposites are especially favored in this regard,
410 owing to their unique versatility that extends their applications from flame retardant and X-ray shields to
411 mechanical reinforcements [78-83].

412 Woven structures (Figures 8a-8i), by nature, have empty space between the warp and weft ribbons, as
413 shown in Figures 8a-8ii. The presence of such pores significantly affects the interaction with polymer, e.g.,
414 epoxy, mainly because the epoxy chains have a high chance of being entangled in these pores and creating
415 an extra mechanical grip between the two structures (Figures 8c-8i-ii). The mechanical prowess of this grip
416 can be evaluated by MD simulations, where an epoxy cluster is moved by applying shear forces over one
417 of these pores. This process for graphene weave is shown in Figure 8c-i-iii.

418 We examine polymer composites reinforced with the same woven 2D materials, i.e., graphene, Mxene,
419 black phosphorous and LDH, and filled with epoxy for interfacial shear strength, with different sliding
420 speed (and corresponding strain rates) over different pore sizes (Figures 8e-h8). The results show that, in
421 general, as the pore size grows, the effect of the mechanical grip increases. For instance, in the case of
422 graphene, increasing the pore diameter from 10 Å to 30 Å translates into an increase in the interfacial shear
423 strength from ~90 to ~200 MPa at a 10 km/s sliding speed. This growth is much more pronounced in the
424 lower sliding speeds; for instance, the corresponding growth for the same transition from 10 A to 30 A at
425 0.1 km/s is 3 to 12 MPa. Similar trends are also accurate for the other nanoribbons.

426 Overall, the results show that the main factors determining the sliding resistance/interfacial shear strength
427 are the ribbon – epoxy non-bonding interactions, especially for the graphene ribbons where the polar
428 oxygen atoms from the epoxy species delocalize the $sp^2$ electrons forming attractive dipoles; this attraction
429 is accompanied by a mechanical grip, where the epoxy molecules can penetrate the woven formation.

430 A closer look at the diagrams shows that Mxene is especially effective in interacting with the epoxy,
431 followed by graphene and LDH. Black phosphorous shows the lowest interfacial shear strength, where the

presence of pore size has the most significant effect. The inclusion of the pores in the interfacial area between epoxy and black phosphorous nanoribbon multiplies the epoxy–weave cohesion by 9 at 0.1 km/s and 57% at 10 km/s; the same effect is 1.25 at 0.1 km/s and 53% at 10 km/s for graphene. The presence of the pore is more effective at lower sliding speeds. This pattern is observed for all modeled sliding speeds and pore diameters. The synergic effect of epoxy penetrated through the woven formation, and the interweaving friction can significantly enhance the mechanical properties of the woven structure. This can be observed by combining the results from Figure 6 and Figure 8, where the strong interlocked weave and the filling epoxy form a highly ductile and robust structure.

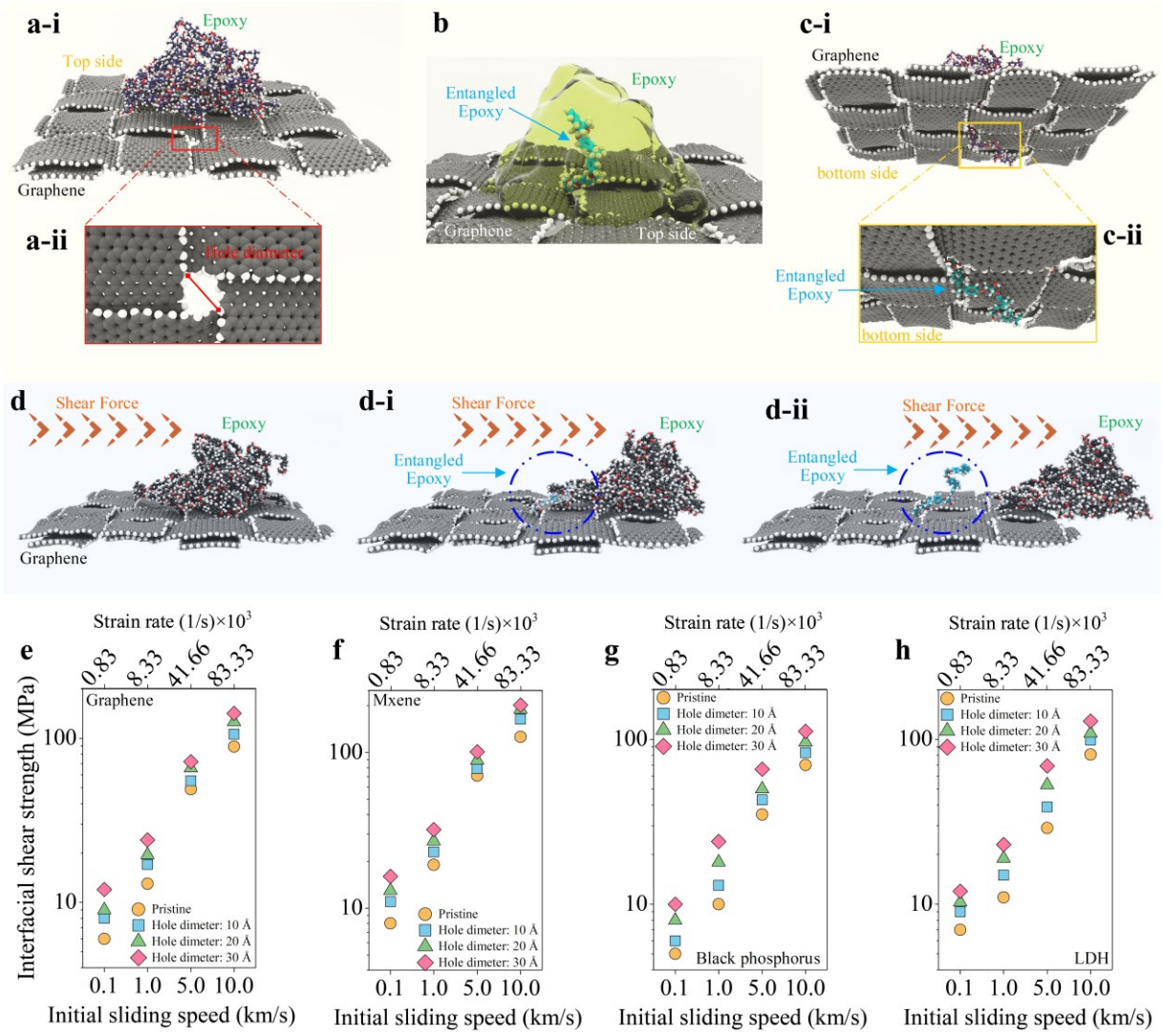

*Figure 8. The epoxy–weave interaction resisting against sliding at corresponding speeds. (a-i) The interaction of graphene weave – epoxy interaction, (a-ii) inevitable pore in the woven pattern, and (b) entangled epoxy within pores in the weave. Entangled epoxy (c-i) from the bottom view and (c-ii) closer view of the entangled segment. (d-d-ii) The sliding entangled epoxy over graphene. Interfacial shear strength for (e) graphene, (f) Mxene, (g) black phosphorous, and (h) LDH – epoxy interactions.*

## Conclusions

In summary, the internal cohesion of a woven network of nanoribbons under extraordinary pull-out action proved to be dependent on interweaving friction, which is a direct product of the interacting nanoribbons' surface and edges in the weave. While the woven pattern is designed to distribute applied stress into the ribbons (i.e., nanosheets), is cohesion depends on the undisrupted formation of the ribbons to act as a unified plane. As a result, the interweaving friction becomes essential to preserving the fabric's cohesion. Our theoretical approach shows that the acting friction is the combination of the interlayer interactions in form of Van der Waals gravitation and a repulsive force in resulted from an aversion to forced spatial confinement (orbital overlap) in the edges of sliding nanosheet (warp) and the confining perpendicular nanosheets (wefts) during extreme vertical loading. As a result, the woven patterns that provide more interacting edges provide higher resistance to the pull-out failure. Among the modeled patterns, the plain-woven pattern showed the most interacting edges, which corresponds with the highest charge transferred as a result of forced orbital overlap, collectively resulting in higher pull-out resistance. This is the case in the interweaving friction between the three modeled forms of weave, plain, Twill, and Satin. The over-under form in the plain form, which runs without skipping over the entire weave, showed the highest interfacial shear strength and resistance against sliding. Apart from interweaving friction, the woven structures also provide inherent pores, arising from the weaving pattern itself, which might contribute to the cohesion of the structures of polymer composite materials. Atop of the nonbonding (physical) interaction with the weave, these epoxy molecules form a mechanical grip by penetrating the woven fabric. Still, the main factor remains within the interacting surface and edges, which depends on the weaving

pattern. In the absence or failure of epoxy as the bonding agent, it is the concentration of restraining force at the edges, i.e. interweaving friction, that sustains the integrity of the weave and the stability of the composite by keeping the movement of the confined nanoribbons in check. The results from this research shed light on friction as the essential guarantor of formation stability in extreme loading conditions. The uncovered interweaving friction mechanism is an essential part of the physical behavior of knots and weaves at the atomic scale, which furthers our understanding of one of the promising fields of precise manufacturing, *i.e.* weaving, and opens new opportunities for developing nanostructures with revolutionary functionalities and performance.

## Declarations


## Funding

This work was supported by the National Science Foundation under Grant 2134465.


## Conflict of interest

The authors declare that they have no conflict of interest.

## Contributions

Mohammad Zakertabrizi and Ehsan Hossieni devised the idea, simulations, original analysis and Writing – original draft. Hamed Fallahi contributed to the simulations and data curing. Terry Creasy and Kenan Song aided in developing and transforming the original idea into models. Ali Tabei, Kyungjun Lee and Amir Razmjou contributed to the data analysis and revisions to the manuscript. Dorrin Jarrahbashi and Amir Asadi led the project and supervised the models, analysis and writing.

## Data availability

Data can be made available on request to the corresponding authors.

## References


1. Tiwari, S.K., et al., *Graphene research and their outputs: Status and prospect.* Journal of Science: Advanced Materials and Devices, 2020. **5**(1): p. 10-29.
2. Yu, W., et al., *Progress in the functional modification of graphene/graphene oxide: A review.* RSC Advances, 2020. **10**(26): p. 15328-15345.

3. Cai, W., et al., *Thermal Transport in Suspended and Supported Monolayer Graphene Grown by Chemical Vapor Deposition.* Nano Letters, 2010. **10**(5): p. 1645-1651.
4. Wei, N., et al., *Thermal rectification of graphene on substrates with inhomogeneous stiffness.* Carbon, 2019. **154**: p. 81-89.
5. Balandin, A.A., et al., *Superior Thermal Conductivity of Single-Layer Graphene.* Nano Letters, 2008. **8**(3): p. 902-907.
6. Gabris, M.A., et al., *Chitosan magnetic graphene grafted polyaniline doped with cobalt oxide for removal of arsenic (V) from water.* Environmental research, 2022. **207**: p. 112209.
7. Hosseini, E., et al., *Mechanical hydrolysis imparts self-destruction of water molecules under steric confinement.* Physical Chemistry Chemical Physics, 2021. **23**(10): p. 5999-6008.
8. Geim, A.K. and K.S. Novoselov, *The rise of graphene*, in *Nanoscience and technology: a collection of reviews from nature journals*. 2010, World Scientific. p. 11-19.
9. Yue, Y., et al., *Highly self-healable 3D microsupercapacitor with MXene–graphene composite aerogel.* Acs Nano, 2018. **12**(5): p. 4224-4232.
10. Wang, C., et al., *Review of recent progress on graphene-based composite gas sensors.* Ceramics International, 2021. **47**(12): p. 16367-16384.
11. Kim, K.S., et al., *Large-scale pattern growth of graphene films for stretchable transparent electrodes.* Nature, 2009. **457**(7230): p. 706-710.
12. Bunch, J.S., et al., *Impermeable Atomic Membranes from Graphene Sheets.* Nano Letters, 2008. **8**(8): p. 2458-2462.
13. Kaynan, O., et al., *Multifunctionality through Embedding Patterned Nanostructures in High-Performance Composites.* Advanced Materials, 2023. **35**(32): p. 2300948.
14. Shi, X., et al., *Improvement of thermal conductivities and simulation model for glass fabrics reinforced epoxy laminated composites via introducing hetero-structured BNN-30@ BNNS fillers.* Journal of Materials Science & Technology, 2021. **82**: p. 239-249.
15. Cai, X., et al., *Matching micro-and nano-boron nitride hybrid fillers for high-thermal conductive composites.* Journal of Applied Polymer Science, 2021. **138**(24): p. 50575.
16. Hosseini, E., et al., *Mechanical and electromechanical properties of functionalized hexagonal boron nitride nanosheet: A density functional theory study.* The Journal of Chemical Physics, 2018. **149**(11): p. 114701.
17. Roudi, M.R.R., et al., *Review of Boron Nitride Nanosheet-Based Composites for Construction Applications.* ACS Applied Nano Materials, 2022. **5**(12): p. 17356-17372.
18. Wei, N., et al., *Knitted graphene-nanoribbon sheet: a mechanically robust structure.* Nanoscale, 2012. **4**(3): p. 785-791.
19. Wei, N., et al., *A heat and force locating sensor with nanoscale precision: a knitted graphene sheet.* Nanoscale, 2021. **13**(11): p. 5826-5833.
20. Reecht, G., et al., *Pulling and stretching a molecular wire to tune its conductance.* The Journal of Physical Chemistry Letters, 2015. **6**(15): p. 2987-2992.
21. Fournier, N., et al., *Force-controlled lifting of molecular wires.* Physical Review B, 2011. **84**(3): p. 035435.
22. Hosseini, E., et al., *Robust cleaning mechanism permanently detaches hydrocarbon species from silicate surfaces by amphiphiles.* Applied Surface Science, 2021. **558**: p. 149954.
23. Zakertabrizi, M., et al., *Turning two waste streams into one solution for enhancing sustainability of the built environment.* Resources, Conservation and Recycling, 2021. **174**: p. 105778.
24. Arzt, E., S. Gorb, and R. Spolenak, *From micro to nano contacts in biological attachment devices.* Proceedings of the National Academy of Sciences, 2003. **100**(19): p. 10603-10606.
25. Gao, H. and H. Yao, *Shape insensitive optimal adhesion of nanoscale fibrillar structures.* Proceedings of the National Academy of Sciences, 2004. **101**(21): p. 7851-7856.

26. Yao, H., et al., *Optimal design of multilayer radar absorbing materials: a simulation-optimization approach.* Advanced Composites and Hybrid Materials, 2023. **6**(1): p. 43.
27. Shkir, M., et al., *Density Functional Theory Studies on a Novel 1-Ethyl-4-phenyl-1,5-benzodiazepin-2-thione Molecule and Its Derivatives for Opto-nonlinear Applications.* Engineered Science, 2022. **19**: p. 319-329.
28. Qin, Z., et al., *Mechanics of micropattern-guided formation of elastic surface instabilities on the polydimethylsiloxane bilayer.* Advanced Composites and Hybrid Materials, 2023. **6**(5): p. 160.
29. Ibitoye, A.I., et al., *Investigation of Photoelectric Properties, Substrate Effects and Structural Identification of Layered Rutile Titanium Oxide with χ3 of Borophene using Density Functional Theory.* Engineered Science, 2022. **20**: p. 364-376.
30. Zhiguo, M., et al., *Co-simulation technology of mold flow and structure for injection molding reinforced thermoplastic composite (FRT) parts.* Advanced Composites and Hybrid Materials, 2022. **5**(2): p. 960-972.
31. R., J., et al., *Density Functional Theory Study of Manganese doped Armchair Graphene Nanoribbon for Effective Carbon Dioxide Gas Sensing.* ES Energy & Environment, 2022. **18**: p. 47-55.
32. Wu, N., et al., *Dielectric properties and electromagnetic simulation of molybdenum disulfide and ferric oxide-modified Ti3C2TX MXene hetero-structure for potential microwave absorption.* Advanced Composites and Hybrid Materials, 2022. **5**(2): p. 1548-1556.
33. Rahimian-Koloor, S.M.R. and M.M. Shokrieh, *Investigating the Effect of the Curing-induced Residual Stress on the Mechanical Behavior of Carbon Nanotube/Epoxy Nanocomposites by Molecular Dynamics Simulation.* Engineered Science, 2023. **22**: p. 817.
34. Sinclair, R.C., J.L. Suter, and P.V. Coveney, *Graphene–graphene interactions: friction, superlubricity, and exfoliation.* Advanced Materials, 2018. **30**(13): p. 1705791.
35. Hod, O., et al., *Structural superlubricity and ultralow friction across the length scales.* Nature, 2018. **563**(7732): p. 485-492.
36. Dietzel, D., et al., *Limitations of structural superlubricity: chemical bonds versus contact size.* Acs Nano, 2017. **11**(8): p. 7642-7647.
37. Gao, X., et al., *Superlubric polycrystalline graphene interfaces.* Nature Communications, 2021. **12**(1): p. 5694.
38. Zheng, X., et al., *Robust ultra-low-friction state of graphene via moiré superlattice confinement.* Nature communications, 2016. **7**(1): p. 1-7.
39. Vazirisereshk, M.R., et al., *Origin of nanoscale friction contrast between supported graphene, MoS2, and a graphene/MoS2 heterostructure.* Nano letters, 2019. **19**(8): p. 5496-5505.
40. Hosseini, E., et al., *Orbital overlapping through induction bonding overcomes the intrinsic delamination of 3D-printed cementitious binders.* ACS nano, 2020. **14**(8): p. 9466-9477.
41. Cho, D.-H., et al., *Effect of surface morphology on friction of graphene on various substrates.* Nanoscale, 2013. **5**(7): p. 3063-3069.
42. Berman, D., et al., *Nanoscale friction properties of graphene and graphene oxide.* Diamond and Related Materials, 2015. **54**: p. 91-96.
43. Li, H., et al., *Nonmonotonic interfacial friction with normal force in two-dimensional crystals.* Physical Review B, 2020. **102**(8): p. 085427.
44. Guo, Y., W. Guo, and C. Chen, *Modifying atomic-scale friction between two graphene sheets: A molecular-force-field study.* Physical Review B, 2007. **76**(15): p. 155429.
45. Song, Y., et al., *Velocity Dependence of Moiré Friction.* Nano Letters, 2022. **22**(23): p. 9529-9536.
46. Hosseini, E., et al., *Graphene oxide in ceramic-based layered structure: Nanosheet optimization.* Construction and Building Materials, 2019. **224**: p. 266-275.

47. Sun, H., *COMPASS: an ab initio force-field optimized for condensed-phase applications overview with details on alkane and benzene compounds.* The Journal of Physical Chemistry B, 1998. **102**(38): p. 7338-7364.
48. Zhang, T., et al., *Parameterization of a COMPASS force field for single layer blue phosphorene.* Nanotechnology, 2020. **31**(14): p. 145702.
49. Chen, W.-H., et al., *Mechanical property assessment of black phosphorene nanotube using molecular dynamics simulation.* Computational Materials Science, 2017. **133**: p. 35-44.
50. Chen, S.J., et al., *Reinforcing mechanism of graphene at atomic level: Friction, crack surface adhesion and 2D geometry.* Carbon, 2017. **114**: p. 557-565.
51. Arshadi, F., et al., *The effect of D-spacing on the ion selectivity performance of MXene membrane.* Journal of Membrane Science, 2021. **639**: p. 119752.
52. Rappé, A.K., et al., *UFF, a full periodic table force field for molecular mechanics and molecular dynamics simulations.* Journal of the American chemical society, 1992. **114**(25): p. 10024-10035.
53. Ding, L., et al., *MXene molecular sieving membranes for highly efficient gas separation.* Nature communications, 2018. **9**(1): p. 1-7.
54. Ding, L., et al., *Effective ion sieving with Ti3C2Tx MXene membranes for production of drinking water from seawater.* Nature Sustainability, 2020. **3**(4): p. 296-302.
55. Abdollahzadeh, M., et al., *Low humid transport of anions in layered double hydroxides membranes using polydopamine coating.* Journal of Membrane Science, 2021. **624**: p. 118974.
56. Heinz, H., et al., *Thermodynamically consistent force fields for the assembly of inorganic, organic, and biological nanostructures: the INTERFACE force field.* Langmuir, 2013. **29**(6): p. 1754-1765.
57. Lin, T.-J. and H. Heinz, *Accurate force field parameters and pH resolved surface models for hydroxyapatite to understand structure, mechanics, hydration, and biological interfaces.* The Journal of Physical Chemistry C, 2016. **120**(9): p. 4975-4992.
58. Zhang, L., W. Ji, and K. Liew, *Mechanical properties of diamond nanothread reinforced polymer composites.* Carbon, 2018. **132**: p. 232-240.
59. Ji, W.-M., L.-W. Zhang, and K. Liew, *Understanding interfacial interaction characteristics of carbon nitride reinforced epoxy composites from atomistic insights.* Carbon, 2021. **171**: p. 45-54.
60. Basquiroto de Souza, F., et al., *Controlled growth and ordering of poorly-crystalline calcium-silicate-hydrate nanosheets.* Communications Materials, 2021. **2**(1): p. 1-11.
61. Rad, A.S., et al., *Lewis acid-base surface interaction of some boron compounds with N-doped graphene; first principles study.* Current Applied Physics, 2015. **15**(10): p. 1271-1277.
62. Abdollahzadeh, M., et al., *Designing Angstrom-Scale Asymmetric MOF-on-MOF Cavities for High Monovalent Ion Selectivity.* Advanced Materials, 2022. **34**(9): p. 2107878.
63. Viani, L., C. Curutchet, and B. Mennucci, *Spatial and electronic correlations in the PE545 light-harvesting complex.* The journal of physical chemistry letters, 2013. **4**(3): p. 372-377.
64. Mennucci, B., *Modeling environment effects on spectroscopies through QM/classical models.* Physical Chemistry Chemical Physics, 2013. **15**(18): p. 6583-6594.
65. Wang, X., C. Lu, and M. Yang, *the impact of electron correlation on Describing QM/MM interactions in the Attendant Molecular Dynamics Simulations of co in Myoglobin.* Scientific reports, 2020. **10**(1): p. 1-12.
66. Wang, J.-N., et al., *Accelerated Computation of Free Energy Profile at Ab Initio Quantum Mechanical/Molecular Mechanics Accuracy via a Semiempirical Reference Potential. 4. Adaptive QM/MM.* Journal of chemical theory and computation, 2021. **17**(3): p. 1318-1325.
67. Hohenberg, P. and W. Kohn, *Inhomogeneous electron gas.* Physical review, 1964. **136**(3B): p. B864.
68. Kohn, W. and L.J. Sham, *Self-consistent equations including exchange and correlation effects.* Physical review, 1965. **140**(4A): p. A1133.

69. Roothaan, C.C.J., *New Developments in Molecular Orbital Theory.* Reviews of Modern Physics, 1951. **23**(2): p. 69-89.
70. Perdew, J.P., K. Burke, and M. Ernzerhof, *Generalized Gradient Approximation Made Simple.* Physical Review Letters, 1996. **77**(18): p. 3865-3868.
71. Aramfard, M., et al., *Aqueous dispersion of carbon nanomaterials with cellulose nanocrystals: an investigation of molecular interactions.* Small, 2022. **18**(37): p. 2202216.
72. Abraham, J., et al., *Tunable sieving of ions using graphene oxide membranes.* Nature nanotechnology, 2017. **12**(6): p. 546-550.
73. Lei, Y.-J., et al., *Tailoring MXene-based materials for sodium-ion storage: synthesis, mechanisms, and applications.* Electrochemical Energy Reviews, 2020. **3**(4): p. 766-792.
74. Tang, J., et al., *Interlayer space engineering of MXenes for electrochemical energy storage applications.* Chemistry–A European Journal, 2021. **27**(6): p. 1921-1940.
75. Pan, D., et al., *Simulations of twisted bilayer orthorhombic black phosphorus.* Physical Review B, 2017. **96**(4): p. 041411.
76. Shulenburger, L., et al., *The nature of the interlayer interaction in bulk and few-layer phosphorus.* Nano letters, 2015. **15**(12): p. 8170-8175.
77. Liu, Y., et al., *Molecular sieving through interlayer galleries.* Journal of Materials Chemistry A, 2014. **2**(5): p. 1235-1238.
78. Li, Z., et al., *Boron nitride whiskers and nano alumina synergistically enhancing the vertical thermal conductivity of epoxy-cellulose aerogel nanocomposites.* Advanced Composites and Hybrid Materials, 2023. **6**(6): p. 224.
79. Li, X., et al., *Electrophoretically deposited "rigid-flexible" hybrid graphene oxide-polyethyleneimine on carbon fibers for synergistically reinforced epoxy nanocomposites.* Advanced Composites and Hybrid Materials, 2023. **6**(4): p. 152.
80. Zhao, M., et al., *Stepwise assembling manganese dioxide nanosheets and metal-organic frameworks on carbon fiber for deriving desirable mechanical properties and flame retardancy of epoxy composites.* Advanced Composites and Hybrid Materials, 2023. **6**(4): p. 150.
81. Sun, Y., et al., *Effects of stitch yarns on interlaminar shear behavior of three-dimensional stitched carbon fiber epoxy composites at room temperature and high temperature.* Advanced Composites and Hybrid Materials, 2022. **5**(3): p. 1951-1965.
82. Ye, X.-Y., et al., *Sustainable wearable infrared shielding bamboo fiber fabrics loaded with antimony doped tin oxide/silver binary nanoparticles.* Advanced Composites and Hybrid Materials, 2023. **6**(3): p. 106.
83. Wang, W., et al., *Lead-free and wearing comfort 3D composite fiber-needled fabric for highly efficient X-ray shielding.* Advanced Composites and Hybrid Materials, 2023. **6**(2): p. 76.